Check for updates

In situ fabrication of MIL-68(In)@ZnIn₂S₄ heterojunction for enhanced photocatalytic hydrogen production†

Mengxi Tan,[a,b] Chengye Yu,[a,b] Hua Zeng,[a,b] Chuanbao Liu,[a,c] Wenjun Dong,[a,c] Huimin Meng,[b] Yanjing Su, [ID][a,b] Lijie Qiao,[a,b] Lei Gao, [ID][a,b] Qipeng Lu [ID][c] and Yang Bai [ID] ⋆[a,b]

Metal–organic frameworks (MOFs), as a class of semiconductor-like materials, are widely used in photocatalysis. However, the limited visible light absorption and poor charge separation efficiency are the main challenges restricting their photocatalytic performance. Herein, the type II heterojunction MIL-68(In)@ZIS was successfully fabricated by *in situ* growth of ZnIn₂S₄ (ZIS) on the surface of a representative MOF, *i.e.* MIL-68(In). After composition optimization, MIL-68(In)-20@ZIS shows an extraordinary photocatalytic hydrogen production efficiency of 9.09 mmol g⁻¹ h⁻¹ and good photochemical stability, which far exceeds those of most photocatalysts. The hierarchical loose structure of MIL-68(In)-20@ZIS is conducive to the adsorption of reactants and mass transfer. Meanwhile, a large number of tight 2D contact interfaces significantly reduce the obstruction of charge transfer, paving the way for high-perform photocatalytic hydrogen evolution. The experimental results demonstrate that the MIL-68(In)@ZIS heterojunction achieves intensive photoresponse and effective charge separation and transfer benefiting from unique charge transport paths of a type II heterojunction. This study opens an avenue toward MOF-based heterojunctions for solar energy conversion.

1 Introduction

As a promising renewable energy source, hydrogen energy has the advantages of high calorific value, environmental friendliness and abundant raw materials.[1] However, the hydrogen production methods of methane steam reforming, coal coking/gasification and electrolysis of water rely heavily on fossil energy sources and have high requirements for equipment.[2,3] Photocatalytic hydrogen production converts solar energy into chemical energy in a green and clean way, which is expected to alleviate the current energy crisis and environmental pollution problems.[4,5] Up to now, numerous studies on photocatalysts, such as metal sulfides,[6,7] metal oxides,[8] polymers,[9] carbon materials,[10–12] and so on, have contributed significantly to the development of photocatalytic technology. However, the poor

separation efficiency of photogenerated charges poses a considerable challenge for the application of photocatalytic hydrogen production. Various strategies have been developed to address this issue, such as defects engineering,[13] morphology tuning[1] and heterojunction construction.[14] Among them, the design of composite photocatalyst to construct heterojunction is an effective means to achieve the separation of photogenerated carriers, which makes full use of the excellent properties of each component.

In the last few decades, metal–organic frameworks (MOFs), self-assembled from metal ions or metal clusters with organic ligands, have attracted extensive attention due to their widespread application prospect in gas storage and separation,[15] drug delivery,[16] fluorescent sensors,[17] photocatalytic pollutant degradation[18] and energy production.[19] Compared with traditional semiconductors, MOFs possess high porosity, large specific surface area, adjustable pore size and structural diversity required for photocatalytic reactions, as well as simple synthesis, making MOFs an ideal candidate for photocatalytic materials.[20–22] Therefore, MOFs are expected to become a popular material in the field of environment and energy in the future. However, the photocatalytic activity of MOFs is largely limited by poor charge separation and transfer efficiency, inferior photochemical stability and weak photoresponse capacity. To overcome the low photocatalytic performance, the

[a]Beijing Advanced Innovation Center for Materials Genome Engineering, University of Science and Technology Beijing, Beijing 100083, China.
E-mail: baiy@mater.ustb.edu.cn
[b]Institute for Advanced Material and Technology, University of Science and Technology Beijing, Beijing 100083, China
[c]School of Materials Science and Engineering, University of Science and Technology Beijing, Beijing 100083, China
†Electronic supplementary information (ESI) available. See DOI: https://doi.org/10.1039/d2nr07017k

construction of heterojunction is widely used by integrating MOFs and semiconductors with well-matched band structure. Recently, Zhang *et al.* demonstrated that the reduction in the density of states for $ZnIn_2S_4$ (ZIS) after adsorption of organic ligands from MOFs effectively inhibits the recombination of charge carriers, thus improving the photocatalytic activity.[23] The g-C_3N_4/MIL-68(In)-NH_2 heterojunction exhibits an extraordinary photocatalytic performance for the degradation of ibuprofen (0.01739 min^{-1}).[24] By combining MIL-125-NH_2 and metal oxides (MoO_3 and V_2O_5) with suitable band structure, Zhang *et al.* proved the importance of built-in electric field induced by energy band bending for enhancing photocatalytic hydrogen production performance.[25] In addition, the 3D hollow BiOBr@Bi-MOF heterostructure was synthesized using BiOBr as a self-sacrificial template for efficient photocatalytic degradation of dyes.[26] To the best of our knowledge, ZIS, which is widely applicable for photocatalytic hydrogen production, is a good candidate for combination with photoactive MIL-68(In) due to its suitable band structure and low toxicity.[27–29]

Motivated by the above studies, we innovatively combined ZIS and MIL-68(In) to construct type II heterojunction with high photocatalytic hydrogen production activity (9.09 mmol g^{-1} h^{-1}) by a low-temperature hydrothermal method. Various characterization approaches were used to study the phase structure, microscopic morphology, light absorption ability and photoelectrochemical performance of MIL-68(In)@ZIS. Experimental results show that the *in situ* growth of 2D ZIS nanoflakes on MIL-68(In) substrates to construct heterojunctions can effectively avoid the agglomeration of ZIS and expose more catalytic active sites. Furthermore, the type II heterojunction MIL-68(In)@ZIS provides a remarkable separation of photogenerated carriers to improve photocatalytic activity, and exhibits excellent stability and reusability. In addition, the underlying mechanism for enhanced photocatalytic hydrogen production performance is explored.

2 Experiments

2.1 Materials

Chemical reagents were used as received without further purification, including glycerol ($C_3H_8O_3$, Sigma-Aldrich, 99.5%), indium chloride hydrate ($InCl_3 \cdot 4H_2O$, Sigma-Aldrich, 97.0%), indium nitrate hydrate ($In(NO_3)_3 \cdot 4.5H_2O$, Aladdin, 99.5%), triethanolamine ($C_6H_{15}NO_3$, Aladdin, 99.0%), thioacetamide (C_2H_5NS, Sigma-Aldrich, 99%), zinc chloride ($ZnCl_2$, Sigma-Aldrich, 99.999%), 2-aminoterephthalic acid ($C_8H_7NO_4$, Aladdin, 98.0%), N,N-dimethylformamide (C_3H_7NO, Aladdin, 99.9%), 5,5-dimethyl-1-pyrroline N-oxide ($C_6H_{11}NO$, Aladdin, 97%) and 2,2,6,6-tetramethylpiperidinooxy ($C_9H_{18}NO$, Aladdin, 99%).

2.2 Synthesis of MIL-68(In)

MIL-68(In) was prepared by solvothermal method and the detailed preparation processes are as follows: 0.598 g of $In(NO_3)_3 \cdot 4.5H_2O$ and 0.234 g of $C_8H_7NO_4$ were dissolved

in 20 mL N,N-dimethylformamide (DMF) with magnetic stirring for 3 h. The homogeneous mixture was transferred into a Teflon liner with a stainless steel autoclave and maintained at 125 °C for 5 h. After natural cooling to room temperature, the synthesized samples were washed several times with ethanol and dried overnight in a vacuum oven at 60 °C to obtain MIL-68(In) samples.

2.3 Synthesis of ZIS

0.055 g $ZnCl_2$ (0.4 mmol), 0.234 g $InCl_3 \cdot 4H_2O$ (0.8 mmol) and 0.24 g C_2H_5NS (3.2 mmol) were dissolved in 40 mL deionized water containing 20 vol% glycerol and stirred for 0.5 h. The mixture was stirred and reacted in a water bath at 80 °C for 2 h. After cooling down to room temperature, the products were washed with deionized water and ethanol several times, and then dried at 60 °C overnight. The prepared samples were marked as ZIS.

2.4 Synthesis of MIL-68(In)@ZIS

The preparation method of MIL-68(In)@ZIS samples is similar to that of ZIS. In detail, a certain amount of MIL-68(In) was ultrasonically dispersed into the aqueous solution (40 mL, 20 vol% glycerol) for 0.5 h. After that, 0.055 g $ZnCl_2$ (0.4 mmol), 0.234 g $InCl_3 \cdot 4H_2O$ (0.8 mmol) and 0.24 g C_2H_5NS (3.2 mmol) were dissolved in the solution and stirred for 1 h. Finally, the acquired solution was stirred and reacted in a water bath at 80 °C for 2 h. The products were washed and then dried at 60 °C overnight. The synthesized samples were labeled as MIL-68(In)-x@ZIS, and x represents the mass (mg) of MIL-68 (In), x = 0, 5, 10, 15, 20, 25, 60. The MIL-68(In)-20/ZIS represents the physical mixture of MIL-68(In) and ZIS.

2.5 Photocatalytic performance test

The photocatalytic hydrogen evolution experiments were carried out in a sealed quartz flask (50 mL). In a typical test, the photocatalyst (5 mg) was added to the 20 mL triethanolamine aqueous solution (20 vol%) with ultrasonic dispersion for 5 min. Before irradiation at room temperature, the reactor was evacuated and filled with N_2 to ensure it kept in an anaerobic condition. The 300 W Xenon lamp equipped with a UV cut-off filter (λ > 400 nm) was adopted as the light source. The evolved H_2 was analyzed by a gas chromatograph (SHIMADZU GC-2014, TCD). The apparent quantum efficiency (AQE) was measured at monochromatic wavelengths (400 nm, 420 nm, 450 nm, 500 nm and 550 nm), and calculated according to the following equation:

$$\text{AQE} = \frac{N_e}{N_p} \times 100\% = \frac{2N_{H_2}N_A hc}{WSt\lambda} \times 100\%$$

where N_e represents the number of electrons participating in the reaction, N_p means the number of incident photons. N_{H_2}, N_A, h and c represent the number of evolved H_2 molecules, Avogadro constant, Planck constant and the speed of light, respectively. W, S, t and λ represent the irradiation intensity, irradiation area, reaction time and the wavelength of monochromatic light, respectively.

3 Results and discussion

3.1 Materials characterization

The preparation process of MIL-68(In)@ZIS is shown in Fig. 1a. First, MIL-68(In) was synthesized by a solvothermal method. Subsequently, 2D ZIS was *in situ* grown on the surface of MIL-68(In) by the low-temperature hydrothermal method. Finally, the layered hybrid photocatalyst MIL-68(In)@ZIS was successfully prepared. Fig. 1b provides the X-ray diffraction (XRD) patterns of MIL-68(In) and MIL-68(In)-x@ZIS (x = 0, 5, 10, 15, 20, 25, 60, x denotes the mass (mg) of MIL-68(In). The XRD pattern of MIL-68(In) is consistent with those reported in literature, demonstrating the successful synthesis of MIL-68 (In).[24] It can be seen that the diffraction peaks of ZIS are in accordance with the crystal structure of hexagonal $ZnIn_2S_4$ (JCPDS no. 65-2023).[30] The FTIR spectra were tested to reveal the surface functional groups of photocatalysts. As displayed in Fig. 1c, the peak located near 3420 cm^{-1} is associated with the stretching vibration of HO–H groups in adsorbed water

molecules.[31] The characteristic peak at 1621 cm^{-1} corresponds to the hydroxyl groups adsorbed on the surface of photocatalysts, while peaks at 1160 and 1099 cm^{-1} are ascribed to the stretching vibration of C–H and C–O bonds in the benzene ring.[23] The results of FTIR spectra corroborate the presence of organic ligands and further prove the synthesis of MIL-68(In). The coexistence of the characteristic signals of MIL-68(In) and ZIS in the XRD and FTIR results of MIL-68(In)-x@ZIS proves the good combination of two components. The morphologies of MIL-68(In) and MIL-68(In)-20@ZIS are shown in Fig. 1d–h. The scanning electron microscopy (SEM) images (Fig. 1d and e) confirm that MIL-68(In) has a uniform diameter and length, and a flocculent layer consisting of 2D ZIS nanoflakes is formed on the surface of MIL-68(In) after low-temperature hydrothermal synthesis. The pure ZIS is a spherical flower shape formed by 2D nanosheets (Fig. S1†). The transmission electron microscopy (TEM) image (Fig. 1f) further demonstrates the layered structure of MIL-68(In)-20@ZIS. The corresponding high-resolution TEM image (HRTEM, Fig. 1g) indi-
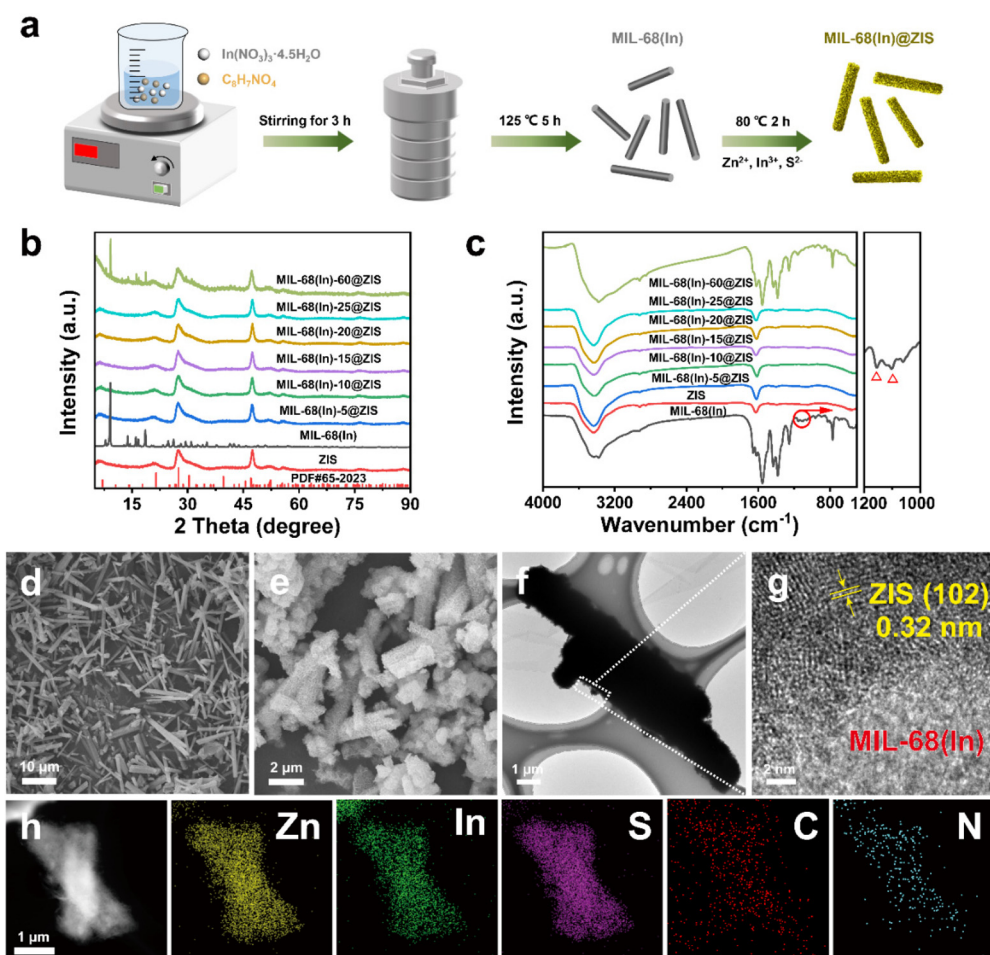

Fig. 1 Synthesis and characterization of MIL-68(In)@ZIS. (a) schematic diagram of the fabrication process for MIL-68(In)@ZIS; (b) XRD patterns of MIL-68(In) and MIL-68(In)-x@ZIS, x represents the mass (mg) of MIL-68(In), x = 0, 5, 10, 15, 20, 25, 60; (c) FTIR spectra of MIL-68(In) and MIL-68(In)-x@ZIS; SEM images of (d) MIL-68(In) and (e) MIL-68(In)-20@ZIS; (f) TEM and (g) HRTEM images of MIL-68(In)-20@ZIS; (h) high-angle annular dark-field scanning TEM (HAADF-STEM) image and corresponding elements mapping of MIL-68(In)-20@ZIS, yellow, green, purple, red, and blue represent Zn, In, S, C and N elements, respectively.

cates that there is a clear heterointerface between ZIS and MIL-68(In). The distinct lattice stripes with an interlayer spacing of 0.32 nm agree well with the (102) plane of ZIS.[32] The amorphous morphology corresponds to MIL-68(In). Furthermore, the corresponding elements mapping (Fig. 1h) shows that MIL-68(In)-20@ZIS is composed of Zn, In, S, C and N elements in uniform distributions, indicating the successful integration of ZIS and MIL-68(In).

The interfacial interaction between MIL-68(In) and ZIS was investigated by X-ray photoelectron spectroscopy (XPS). As observed in Fig. 2a, the major elements in MIL-68(In) are In, N and O, and ZIS primarily contains Zn, In and S elements. The hybrid photocatalyst MIL-68(In)-20@ZIS consists of all the above elements. Fig. 2b displays the high-resolution XPS spectra of In 3d in different samples. The characteristic peaks at 445.40 and 453.02 eV are ascribed to the In $3d_{5/2}$ and In $3d_{3/2}$ in MIL-68(In).[23] As for ZIS, the peaks appeared at 445.26 and 452.76 eV are attributed to the In^{3+}.[33] After the combination of MIL-68(In) and ZIS, the characteristic peaks of In 3d in MIL-68(In)-20@ZIS shift to the direction of low binding energy. As discerned in Fig. 2c, the high-resolution XPS spectra of Zn 2p in ZIS can be deconvoluted into two peaks at 1021.97 and 1045.11 eV, which correspond to Zn $2p_{3/2}$ and Zn $2p_{1/2}$, respectively.[34] It is found that the binding energies of Zn 2p in MIL-68(In)-20@ZIS slightly increase compared to that of pristine ZIS. The high-resolution S 2p XPS spectra confirm the −2 valence of S anions in ZIS.[35] The S 2p spectra are resolved into two peaks at 161.89 and 162.99 eV corresponding to the S $2p_{3/2}$ and S $2p_{1/2}$ of S^{2-} anions in MIL-68(In)-20@ZIS.[36] Notably, MIL-68(In)-20@ZIS has the higher binding energies of S 2p than ZIS. Based on the above analyses, the characteristic peaks of In 3d in MIL-68(In)-20@ZIS migrate to the direction of low binding energy compared with those of single-phase photocatalysts, while signal peaks of Zn 2p and S 2p move in the opposite direction. This phenomenon provides evidence for a strong charge interaction between two components of ZIS and MIL-68(In), which facilitates charge transfer in photocatalytic reactions. In addition, Fig. S2† shows the C 1s XPS spectra of ZIS, MIL-68(In) and MIL-68(In)-20@ZIS. Due to the lack of C element in ZIS, the C 1s high-resolution XPS spectra of ZIS only show the peak located at 284.80 eV belonging to the surface introduced carbon.[24] The C 1s XPS spectra of MIL-68(In) are fitted to two peaks located at 284.80 and 288.88 eV, which are assigned to the C–C bond of surface adventitious carbon and O–C═O bond originated from carboxylate groups in MIL-68(In), respectively.[24] The characteristic peak at 288.88 eV corresponding to carboxyl functional groups of MIL-68(In) can be clearly observed in the C 1s XPS spectra of MIL-68(In)-20@ZIS, which further confirms the combination of ZIS and MIL-68(In) in MIL-68(In)-20@ZIS.
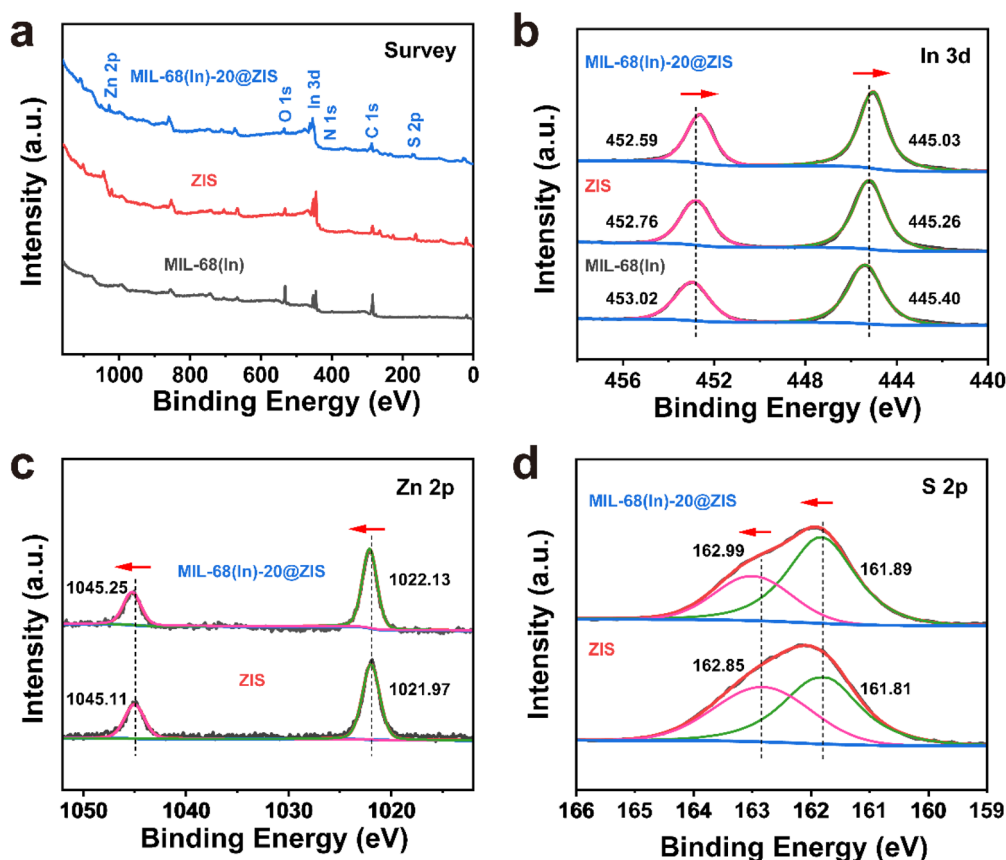

Fig. 2 The XPS spectra of MIL-68(In), ZIS and MIL-68(In)-20@ZIS. (a) survey, (b) In 3d, (c) Zn 2p and (d) S 2p.

3.2 Photocatalytic performance

The photocatalytic hydrogen evolution performance of photo-catalysts was estimated under visible light irradiation in the presence of triethanolamine (TEOA) as sacrificial agent. As shown in Fig. 3a, the pure ZIS exhibits a photocatalytic hydrogen production activity with 4.72 mmol g^{-1} h^{-1}. The hybrid photocatalyst MIL-68(In)@ZIS presents a photocatalytic hydrogen production performance better than ZIS, and the photo-catalytic hydrogen production efficiencies of MIL-68(In)-5@ZIS, MIL-68(In)-10@ZIS, MIL-68(In)-15@ZIS, MIL-68(In)-20@ZIS, MIL-68(In)-25@ZIS and MIL-68(In)-60@ZIS are 5.08, 6.22, 6.34, 9.09, 5.85 and 5.24 mmol g^{-1} h^{-1}, respectively. As

the amount of MIL-68(In) increases, the abundant contact interfaces between MIL-68(In) and ZIS provide a large number of wide and short paths for directional charge transfer, which effectively improves the hydrogen production activity of hybrid photocatalysts. However, excessive MIL-68(In) can lead to the agglomeration of photocatalysts, resulting in decreased hydrogen production performance. Therefore, MIL-68(In)-20@ZIS exhibits the best photocatalytic hydrogen evolution performance (9.09 mmol g^{-1} h^{-1}) among MIL-68(In)-x@ZIS, which has a noticeable advantage in recent works (details see the comparison in Fig. 3b and Table 1). As displayed in Fig. S3,† MIL-68(In)-20/ZIS (the physical mixture of MIL-68(In) and ZIS) has a significantly lower photocatalytic efficiency (4.81 mmol
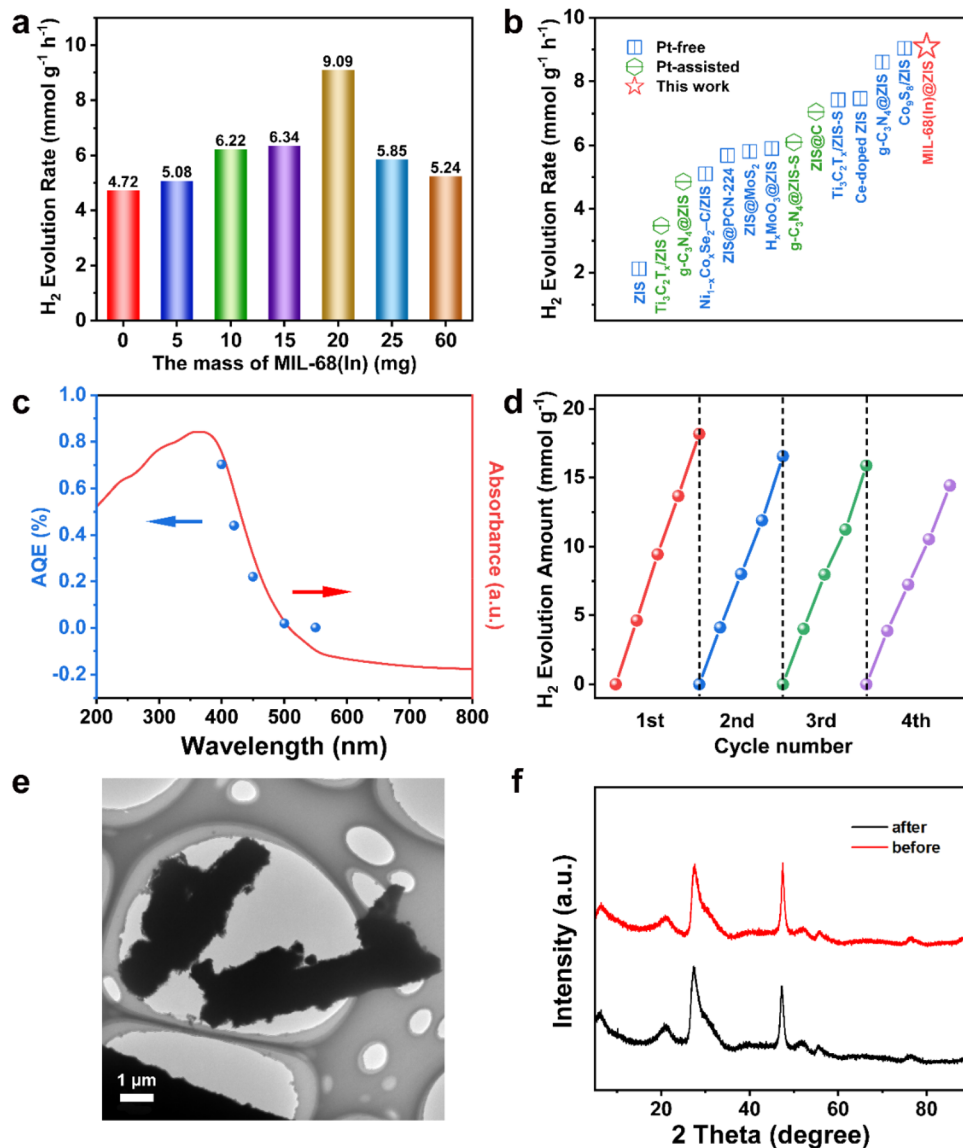

Fig. 3 Photocatalytic hydrogen production performance of photocatalysts. The photocatalytic hydrogen evolution rates of (a) MIL-68(In)-x@ZIS; (b) comparison of the hydrogen production rates of MIL-68(In)-20@ZIS in this work with those of representative photocatalysts reported recently; (c) the wavelength-dependent AQE of MIL-68(In)-20@ZIS; (d) durability test of MIL-68(In)-20@ZIS for four cycles; (e) TEM image after cycles and (f) XRD patterns before and after cycles for MIL-68(In)-20@ZIS.

Table 1 List of the photocatalytic hydrogen production performance of photocatalysts in related systems

Photocatalyst	Sacrificial agent	Cocatalyst/sensitizer	Activity (mmol g^{-1} h^{-1})	Light source	Ref.
ZIS	Na_2S (0.35 M), Na_2SO_3 (0.25 M)	—	2.120	300 W Xe lamp ($\lambda > 420$ nm)	37
$Ti_3C_2T_x$/ZIS	10 vol% TEOA	Pt	3.475	LED lamps ($\lambda > 420$ nm)	27
g-C_3N_4@ZIS	TEOA	Pt	4.854	300 W Xe lamp ($\lambda > 400$ nm)	32
$Ni_{1-x}Co_xSe_2$–C/ZIS	20 vol% TEOA	—	5.1	300 W Xe lamp ($\lambda > 420$ nm)	36
ZIS@PCN-224	Na_2S (0.35 M), Na_2SO_3 (0.25 M)	—	5.68	300 W Xe lamp ($\lambda > 420$ nm)	38
ZIS@MoS_2	Na_2S (0.35 M), Na_2SO_3 (0.25 M)	—	5.808	300 W Xe lamp ($\lambda > 320$ nm)	39
H_xMoO_3@ZIS	10 vol% TEOA	—	5.9	300 W Xe lamp ($\lambda > 420$ nm)	40
g-C_3N_4@ZIS-S	20 vol% TEOA	Pt	6.095	300 W Xe lamp ($\lambda > 420$ nm)	41
ZIS@C	DL-Lactic acid	Pt	7.05	300 W Xe lamp ($\lambda > 420$ nm)	42
$Ti_3C_2T_x$/ZIS	20 vol% TEOA	—	7.420	300 W Xe lamp ($\lambda > 400$ nm)	43
Ce-doped ZIS	10 vol% TEOA	—	7.46	300 W Xe lamp ($\lambda > 400$ nm)	44
g-C_3N_4@ZIS	20 vol% TEOA	—	8.601	300 W Xe lamp ($\lambda > 400$ nm)	45
Co_9S_8/ZIS	10 vol% TEOA	—	9.039	300 W Xe lamp ($\lambda > 400$ nm)	28
MIL-68(In)@ZIS	20 vol% TEOA	—	9.09	300 W Xe lamp ($\lambda > 400$ nm)	This work

g^{-1} h^{-1}) than MIL-68(In)-20@ZIS due to the weak interfacial interaction. The photocatalytic property of MIL-68(In) is almost negligible. In addition, the AQE of MIL-68(In)-20@ZIS was also tested under different incident monochromatic light. Fig. 3c demonstrates that the variation of AQE is in good agreement with the light absorption spectrum of MIL-68(In)-20@ZIS, and the detailed values are shown in Table S1.† The photocatalytic stability of MIL-68(In)-20@ZIS for hydrogen production was further assessed by cyclic experiments. As displayed in Fig. 3d, after suffering consecutive four cycles, the photocatalytic hydrogen evolution rate decreases slightly. Moreover, the rod-like structure of MIL-68(In)-20@ZIS remains (Fig. 3e) and the XRD pattern is almost unchanged (Fig. 3f), all of which proves the good photochemical stability of MIL-68 (In)-20@ZIS for efficient hydrogen production.

3.3 Influence factors of photocatalytic activity

The separation and transfer of photogenerated charges are closely related to the properties of the photocatalyst itself.[46] Therefore, a series of relevant spectroscopic and photoelectrochemical characterizations were carried out to reveal the behavior of photogenerated charge carriers.[47] The steady-state photoluminescence (PL) spectroscopy is an effective means to reflect the recombination of photogenerated electron–hole pairs.[48] As displayed in Fig. 4a, the PL emission peak of ZIS is significantly stronger than that of MIL-68(In)-20@ZIS, which indicates the presence of severe photogenerated electron–hole pairs recombination in ZIS.[49,50] In contrast, MIL-68(In)-20@ZIS has a remarkably improved separation efficiency of photogenerated electron–hole pairs, corresponding to its superior photocatalytic performance. The time-resolved PL (TRPL) spectrum is usually used to reflect the charge carrier dynamics of photocatalysts.[51] As shown in Fig. 4b, MIL-68(In)-20@ZIS has a significantly slower exponential decay than ZIS based on the biexponential function fitting. As listed in Table S2,† the average charge lifetime of MIL-68(In)-20@ZIS (3.76 ns) is distinctly longer than that of ZIS (2.03 ns). The prolonged charge lifetime proves the presence of faster charge transfer and more efficient charge separation in MIL-68(In)-20@ZIS. Furthermore, transient photocurrent tests were

employed to assess the photoelectric response of photocatalysts.[52] Fig. 4c shows that the hybrid photocatalyst MIL-68(In)-20@ZIS exhibits more intense photocurrent signals than bare ZIS due to its excellent photoresponse and charge separation efficiency. Charge migration impedance is also one of the main factors affecting photocatalytic efficiency.[53] As discerned in Fig. 4d, MIL-68(In)-20@ZIS has a faster charge transfer process than pure ZIS. According to the linear sweep voltammetry (LSV) measurements, MIL-68(In)-20@ZIS possesses a great potential for photocatalytic hydrogen production, due to its significantly low overpotential and high current density. Nitrogen absorption-desorption curves of ZIS and MIL-68(In)-20@ZIS are similar (Fig. 4f). The Brunauer–Emmett–Teller (BET) specific surface areas of ZIS and MIL-68(In)-20@ZIS are 209.82 and 210.58 m^2 g^{-1} (Table S3†), respectively. Meanwhile, the large pore volumes provide a good condition for mass transfer (Fig. S4†). All the above results consistently support the superior photoelectrochemical performance and charge separation efficiency of hybrid photocatalyst MIL-68(In)@ZIS, which reveals the reason for its prominent photocatalytic hydrogen production activity.

3.4 Photocatalytic mechanism

The UV-vis absorption spectra and Mott–Schottky (M–S) plots were measured to investigate the optical absorption properties and band gap structure of samples.[54] Compared with ZIS, the pristine MIL-68(In) owns a weaker visible light absorption intensity and a smaller absorption range (Fig. 5a). Thus, after the introduction of ZIS, MIL-68(In)-20@ZIS displays an enhanced visible light absorption capacity. Additionally, as shown in Fig. 5b, the band gaps (E_g) of ZIS and MIL-68(In) are calculated to be 2.68 and 2.89 eV according to the Kubelka–Munk theory.[23] To further reveal the photocatalytic hydrogen production mechanism of MIL-68(In)@ZIS, the conduction band potentials (E_{CB}) of ZIS and MIL-68(In) were determined by the M–S test. Fig. 5c and d indicate that the flat-band potentials (E_{fb}) calculated by the extrapolation of M–S curves for ZIS and MIL-68(In) are −1.11 and −0.76 V vs. Ag/AgCl. The positive slope values of M–S plots demonstrate that the fabricated samples of ZIS and MIL-68(In) are both n-type
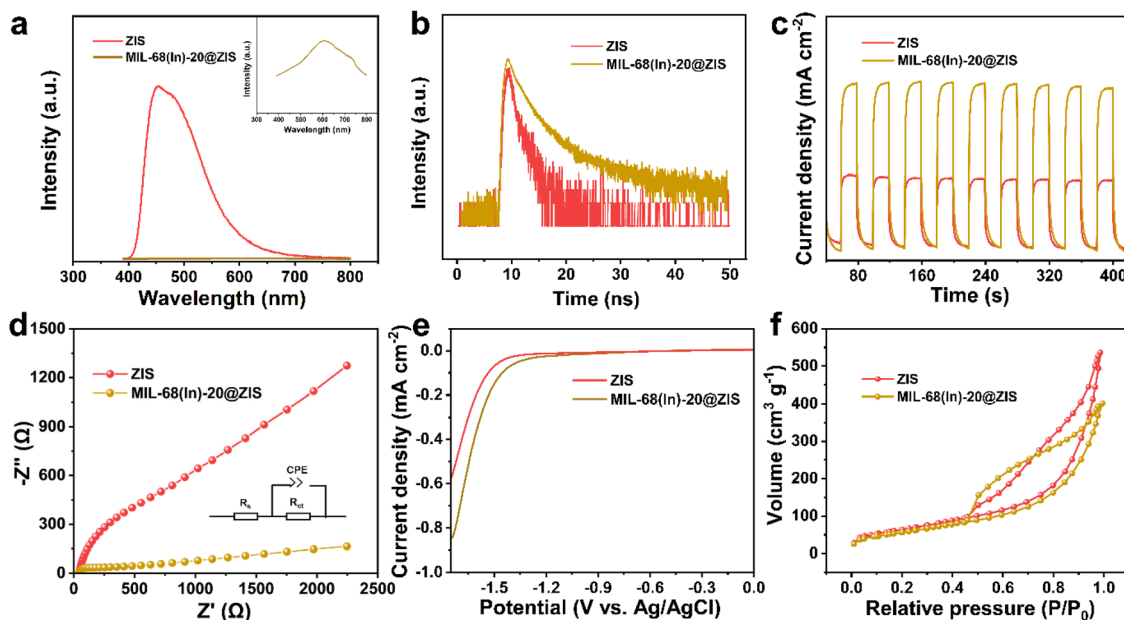
Fig. 4 Photoelectrochemical and physical properties of ZIS and MIL-68(In)-20@ZIS. (a) PL plots; (b) TRPL spectra; (c) transient photocurrent response curves; (d) EIS spectra; (e) LSV curves and (f) nitrogen absorption−desorption isotherms.
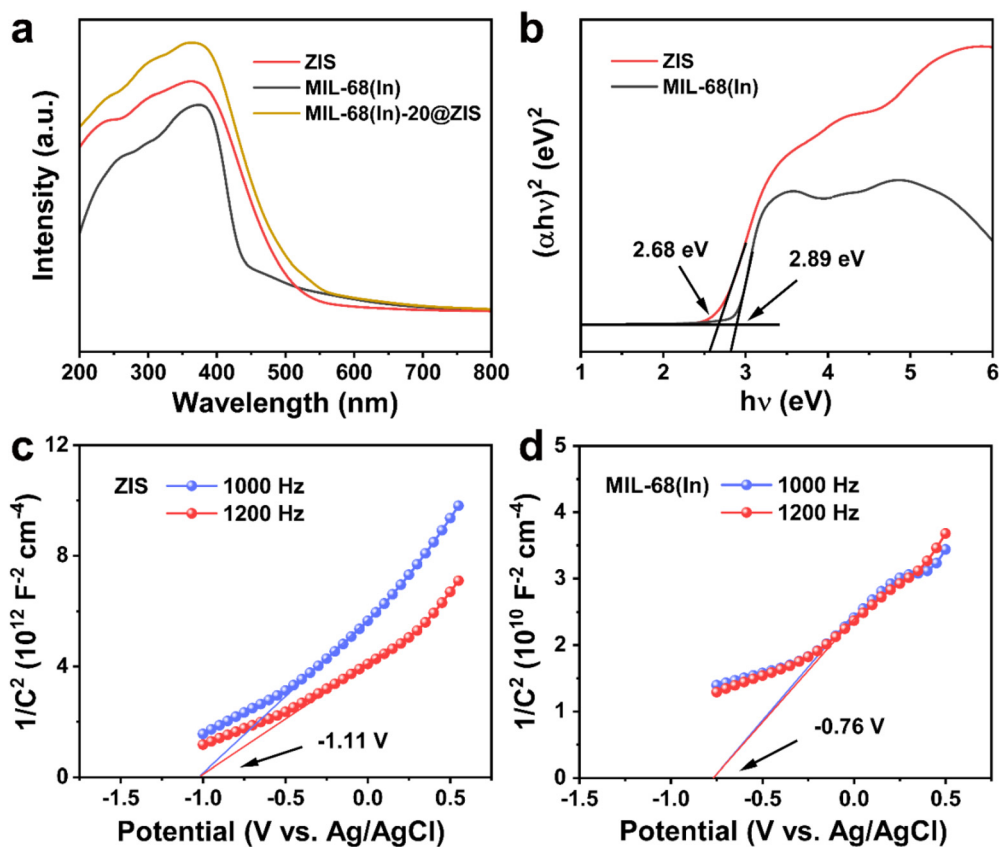

Fig. 5 Energy band structure. (a) UV-vis absorption spectra of ZIS, MIL-68(In) and MIL-68(In)-20@ZIS; (b) Tauc plots of $(\alpha h\nu)^2$ vs. photon energy ($h\nu$) for ZIS and MIL-68(In); M−S plots of (c) ZIS and (d) MIL-68(In).
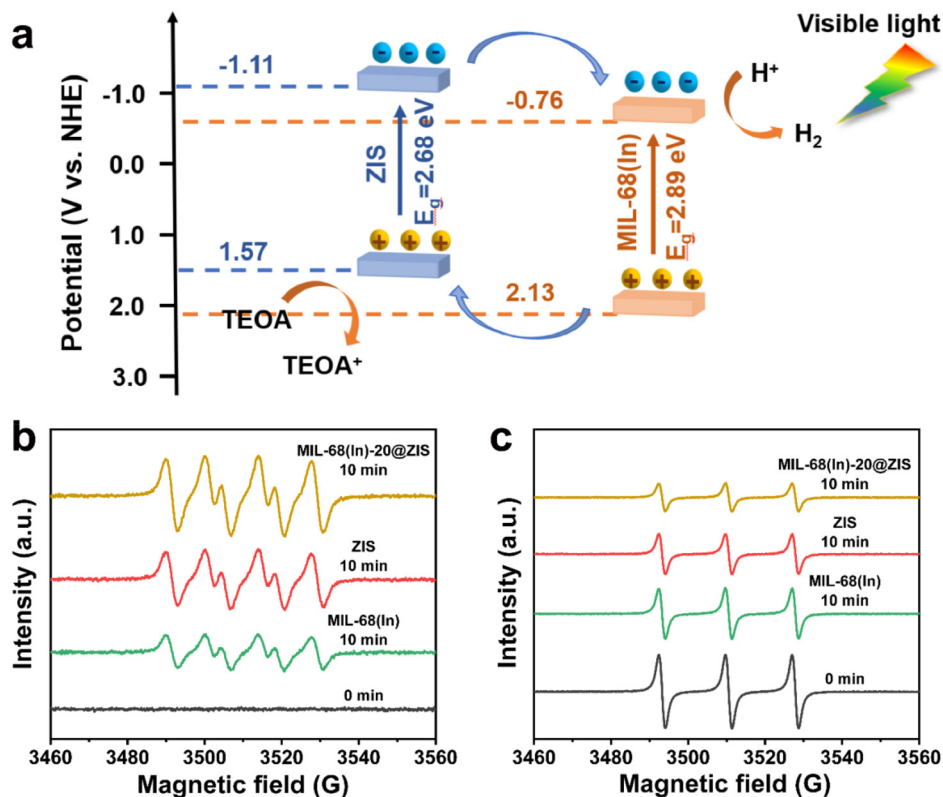
Fig. 6 The photocatalytic mechanism of MIL-68(In)@ZIS. (a) schematic illustration of charge transfer paths for MIL-68(In)@ZIS; EPR spectra of (b) DMPO $^{\cdot}O_2^{-}$ and (c) TEMPO h^{+} for ZIS, MIL-68(In) and MIL-68(In)-20@ZIS.

semiconductors.[55,56] As for n-type semiconductors, the E_{CB} is about 0.2 V lower than E_{fb}.[57] Therefore, the E_{CB} of ZIS and MIL-68(In) are −1.11 and −0.76 V $vs.$ NHE ($E_{NHE} = E_{Ag/AgCl} + 0.197$), respectively.[58] The corresponding valence band potentials (E_{VB}) can be deduced to be 1.57 and 2.13 V $vs.$ NHE according to the equation of $E_{VB} = E_g + E_{CB}$.

Based on the above results, the schematic diagram of charge transfer paths for MIL-68(In)@ZIS is shown in Fig. 6a. The combination of ZIS and MIL-68(In) forms a typical type II heterojunction due to their staggered band gap structure. Under visible light, ZIS and MIL-68(In) absorb photons with sufficient energy and the electrons in their valence band (VB) are excited to the conduction band (CB), leaving photogenerated holes in the VB. Subsequently, driven by the potential difference, the photogenerated electrons in the CB of ZIS migrate towards the CB of MIL-68(In) to participate in the reduction reaction of protons, meanwhile, the holes in the VB of MIL-68(In) reversely transfer to the VB of ZIS to be involved in the oxidation reaction. The effective separation of photogenerated carriers in space is achieved, which facilitates the improvement of photocatalytic hydrogen production performance. To demonstrate the above photocatalytic mechanism, the EPR test was carried out.[27] As shown in Fig. 6b and c, MIL-68(In)-20@ZIS exhibits the stronger DMPO $^{\cdot}O_2^{-}$ (DMPO: 5,5-dimethyl-1-pyrroline N-oxide) signal and weaker TEMPO h^{+} (TEMPO: 2,2,6,6-tetramethylpiperidinooxy) signal than ZIS and

MIL-68(In) under visible light irradiation for 10 min, which corresponds to more separated photoinduced electrons and holes in MIL-68(In)-20@ZIS. The results of EPR test confirm that the type II heterojunction MIL-68(In)-20@ZIS with a staggered band gap structure has a stronger capacity for photogenerated carrier separation, corresponding to the enhancement of photocatalytic activity.

4 Conclusions

In summary, we prepared the hierarchical composite photocatalyst MIL-68(In)@ZIS by a simple low-temperature hydrothermal method, which exploits both the high specific surface area of MIL-68(In) and the good optical properties of ZIS. Under visible light, the optimized photocatalytic performance of MIL-68(In)@ZIS reaches 9.09 mmol g^{-1} h^{-1} with excellent photochemical stability, which has an obvious advantage among related systems. In $situ$ growth of 2D ZIS nanosheets on MIL-68(In) substrates to construct heterojunction can provide abundant surface-active sites and numerous charge transport channels for photocatalytic reactions. The results of experimental characterization indicate that the type II heterojunction MIL-68(In)@ZIS possesses prominent visible light absorption, low charge transfer impedance and fast charge transport, which is essential for improving photocatalytic efficiency. In

addition, energy band structure analyses combined with EPR test confirm the existence of type II heterojunction and reveal its importance for enhanced charge separation efficiency. This work is of great significance for the design and development of high-performance and low-cost photocatalysts for hydrogen production.

Conflicts of interest

There are no conflicts of interest to declare.

Acknowledgements

References

1 M. Tan, Y. Ma, C. Yu, Q. Luan, J. Li, C. Liu, W. Dong, Y. Su, L. Qiao, L. Gao, Q. Lu and Y. Bai, *Adv. Funct. Mater.*, 2022, **32**, 2111740.

2 X. Zou and Y. Zhang, *Chem. Soc. Rev.*, 2015, **44**, 5148–5180.

3 P. Wang, X. Zhang, R. Shi, J. Zhao, Z. Yuan and T. Zhang, *Energy Fuels*, 2022, **36**, 11627–11635.

4 R. Chen, Z. Ren, Y. Liang, G. Zhang, T. Dittrich, R. Liu, Y. Liu, Y. Zhao, S. Pang, H. An, C. Ni, P. Zhou, K. Han, F. Fan and C. Li, *Nature*, 2022, **610**, 296–301.

5 X. Li, Z. Wang and L. Wang, *Small Sci.*, 2021, **1**, 2000074.

6 Q. Lu, Y. Yu, Q. Ma, B. Chen and H. Zhang, *Adv. Mater.*, 2016, **28**, 1917–1933.

7 B. Lin, X. Ren, Z. Chen, H. Xiao, B. Xu, B. Chong and G. Yang, *Nanoscale*, 2022, **14**, 16952–16960.

8 L. Chen, X. Song, J. Ren and Z. Yuan, *Appl. Catal., B*, 2022, **315**, 121546.

9 X. Zhou, Y. Tian, J. Luo, B. Jin, Z. Wu, X. Ning, L. Zhan, X. Fan, T. Zhou, S. Zhang and X. Zhou, *Adv. Funct. Mater.*, 2022, **32**, 2201518.

10 P. Chen, L. Chen, S. Ge, W. Zhang, M. Wu, P. Xing, T. B. Rotamond, H. Lin, Y. Wu and Y. He, *Int. J. Hydrogen Energy*, 2020, **45**, 14354–14367.

11 P. Chen, P. Xing, Z. Chen, X. Hu, H. Lin, L. Zhao and Y. He, *J. Colloid Interface Sci.*, 2019, **534**, 163–171.

12 Q. Zhang, P. Chen, L. Chen, M. Wu, X. Dai, P. Xing, H. Lin, L. Zhao and Y. He, *J. Colloid Interface Sci.*, 2020, **568**, 117–129.

13 X. Ma and H. Cheng, *Appl. Catal., B*, 2022, **314**, 121497.

14 W. Liu, P. Wang, Y. Ao, J. Chen, X. Gao, B. Jia and T. Ma, *Adv. Mater.*, 2022, **34**, 2202508.

15 L. Wu, M. Xue, S. Qiu, G. Chaplais, A. Simon-Masseron and J. Patarin, *Microporous Mesoporous Mater.*, 2012, **157**, 75–81.

16 S. Mallakpour, E. Nikkhoo and C. M. Hussain, *Coord. Chem. Rev.*, 2022, **451**, 214262.

17 S. Wu, H. Min, W. Shi and P. Cheng, *Adv. Mater.*, 2020, **32**, 1805871.

18 C.-C. Wang, J.-R. Li, X.-L. Lv, Y.-Q. Zhang and G. Guo, *Energy Environ. Sci.*, 2014, **7**, 2831–2867.

19 L. Sun, M. Lu, Z. Yang, Z. Yu, X. Su, Y. Lan and L. Chen, *Angew. Chem., Int. Ed.*, 2022, **134**, e202204326.

20 J. Peng, E. Wu, X. Lou, Q. Deng, X. Hou, C. Lv and Q. Hu, *Chem. Eng. J.*, 2021, **418**, 129473.

21 Z. Cai, J. Dai, W. Li, K. B. Tan, Z. Huang, G. Zhan, J. Huang and Q. Li, *ACS Catal.*, 2020, **10**, 13275–13289.

22 Z. Cai, M. Huang, J. Dai, G. Zhan, F. Sun, G. Zhuang, Y. Wang, P. Tian, B. Chen, S. Ullah, J. Huang and Q. Li, *ACS Catal.*, 2022, **12**, 709–723.

23 Q. Zhang, H. Gu, X. Wang, L. Li, J. Zhang, H. Zhang, Y. Li and W. Dai, *Appl. Catal., B*, 2021, **298**, 120632.

24 W. Cao, Y. Yuan, C. Yang, S. Wu and J. Cheng, *Chem. Eng. J.*, 2020, **391**, 123608.

25 C. Zhang, C. Xie, Y. Gao, X. Tao, C. Ding, F. Fan and H. Jiang, *Angew. Chem., Int. Ed.*, 2022, **61**, e202204108.

26 M. Xu, X. Jiang, J. Li, F. Wang, K. Li and X. Cheng, *ACS Appl. Mater. Interfaces*, 2021, **13**, 56171–56180.

27 G. Zuo, Y. Wang, W. Teo, A. Xie, Y. Guo, Y. Dai, W. Zhou, D. Jana, Q. Xian, W. Dong and Y. Zhao, *Angew. Chem., Int. Ed.*, 2020, **59**, 11287–11292.

28 G. Zhang, D. Chen, N. Li, Q. Xu, H. Li, J. He and J. Lu, *Angew. Chem., Int. Ed.*, 2020, **59**, 8255–8261.

29 X. Shi, L. Mao, P. Yang, H. Zheng, M. Fujitsuka, J. Zhang and T. Majima, *Appl. Catal., B*, 2020, **265**, 118616.

30 Q. Luan, X. Xue, R. Li, L. Gu, W. Dong, D. Zhou, X. Wang, B. Li, G. Wang and C. Hou, *Appl. Catal., B*, 2022, **305**, 121007.

31 A. Hassani, A. Khataee, S. Karaca, C. Karaca and P. Gholami, *Ultrason. Sonochem.*, 2017, **35**, 251–262.

32 Z. Gao, K. Chen, L. Wang, B. Bai, H. Liu and Q. Wang, *Appl. Catal., B*, 2020, **268**, 118462.

33 M. Tan, C. Yu, Q. Luan, C. Liu, W. Dong, Y. Su, L. Qiao, L. Gao, Q. Lu and Y. Bai, *J. Mater. Chem. A*, 2022, **10**, 21465–21473.

34 M. Tan, C. Huang, C. Yu, C. Li, R. Yin, C. Liu, W. Dong, H. Meng, Y. Su, L. Qiao, L. Gao, Q. Lu and Y. Bai, *Small*, 2022, **18**, 2205266.

35 W. Zhang, S. Zhao, Y. Xing, H. Qin, Q. Zheng, P. Zhang, S. Zhang and X. Xu, *Chem. Eng. J.*, 2022, **442**, 136151.

36 Y. Chao, P. Zhou, J. Lai, W. Zhang, H. Yang, S. Lu, H. Chen, K. Yin, M. Li, L. Tao, C. Shang, M. Tong and S. Guo, *Adv. Funct. Mater.*, 2021, **31**, 2100923.

37 W. Yang, L. Zhang, J. Xie, X. Zhang, Q. Liu, T. Yao, S. Wei, Q. Zhang and Y. Xie, *Angew. Chem., Int. Ed.*, 2016, **55**, 6716–6720.

38 P. Jin, L. Wang, X. Ma, R. Lian, J. Huang, H. She, M. Zhang and Q. Wang, *Appl. Catal., B*, 2021, **284**, 119762.

39 Y. Peng, M. Geng, J. Yu, Y. Zhang, F. Tian, Y. n. Guo, D. Zhang, X. Yang, Z. Li, Z. Li and S. Zhang, *Appl. Catal., B*, 2021, **298**, 120570.

40 F. Xing, C. Cheng, J. Zhang, Q. Liu, C. Chen and C. Huang, *Appl. Catal., B*, 2021, **285**, 119818.

41 Y. Qin, H. Li, J. Lu, Y. Feng, F. Meng, C. Ma, Y. Yan and M. Meng, *Appl. Catal., B*, 2020, **277**, 119254.

42 H. Li, B. Chong, B. Xu, N. Wells, X. Yan and G. Yang, *ACS Catal.*, 2021, **11**, 14076–14086.

43 T. Su, C. Men, L. Chen, B. Chu, X. Luo, H. Ji, J. Chen and Z. Qin, *Adv. Sci.*, 2022, **9**, 2103715.

44 H. Fan, Y. Jin, K. Liu and W. Liu, *Adv. Sci.*, 2022, **9**, 2104579.

45 H. Yang, R. Cao, P. Sun, J. Yin, S. Zhang and X. Xu, *Appl. Catal., B*, 2019, **256**, 117862.

46 H. Xiao, T. Wei, X. Ren, B. Lin and G. Yang, *Nanoscale*, 2022, **14**, 12403–12408.

47 H. Li, Q. Shen, H. Zhang, J. Gao, H. Jia, X. Liu, Q. Li and J. Xue, *J. Adv. Ceram.*, 2022, **11**, 1873–1888.

48 J. Wang, J. Wang, R. Shi, C. Zhou and T. Zhang, *Small Struct.*, 2023, **4**, 2200105.

49 L. Shang, C. Zhou, T. Bian, H. Yu, L.-Z. Wu, C.-H. Tung and T. Zhang, *J. Mater. Chem. A*, 2013, **1**, 4552–4558.

50 R. Yang, L. Mei, Y. Fan, Q. Zhang, R. Zhu, R. Amal, Z. Yin and Z. Zeng, *Small Methods*, 2021, **5**, 2100887.

51 S. Wang, Y. Wang, S. Zhang, S.-Q. Zang and X. W. Lou, *Adv. Mater.*, 2019, **31**, 1903404.

52 Y. Wang, J. Zhang, X. Cheng, Y. Sha, M. Xu, Z. Su, J. Hu and L. Yao, *Nanoscale*, 2022, **14**, 11012–11017.

53 Y. Ma, Y. Zhang, Y. Ma, T. Lv, B. Xiao, X. Kuang, X. Deng, J. Zhang, J. Zhao and Q. Liu, *Nanoscale*, 2022, **14**, 15889–15896.

54 C. Yu, M. Tan, C. Tao, Y. Hou, C. Liu, H. Meng, Y. Su, L. Qiao and Y. Bai, *J. Adv. Ceram.*, 2022, **11**, 414–426.

55 H. Zhao, J. Liu, C. Li, X. Zhang, Y. Li, Z. Hu, B. Li, Z. Chen, J. Hu and B. Su, *Adv. Funct. Mater.*, 2022, **32**, 2112831.

56 J. Fu, Q. Xu, J. Low, C. Jiang and J. Yu, *Appl. Catal., B*, 2019, **243**, 556–565.

57 Y. Hu, X. Hao, Z. Cui, J. Zhou, S. Chu, Y. Wang and Z. Zou, *Appl. Catal., B*, 2020, **260**, 118131.

58 L. Chen, Y. Xu and B. Chen, *Appl. Catal., B*, 2019, **256**, 117848.